Effect of wing fold angles on the terminal descent velocity of double-winged autorotating seeds, fruits, and other diaspores

Richard A. Fauli, Jean Rabault, and Andreas Carlson*
Department of Mathematics, Mechanics Division, University of Oslo, 0316 Oslo, Norway

(Received 5 December 2018; published 18 July 2019)

Wind dispersal of seeds is an essential mechanism for plants to proliferate and to invade new territories. In this paper we present a methodology used in our recent work [Rabault, Fauli, and Carlson, Phys. Rev. Lett. **122**, 024501 (2019)] that combines 3D printing, a minimal theoretical model, and experiments to determine how the curvature along the length of the wings of autorotating seeds, fruits, and other diaspores provides them with an optimal wind dispersion potential, i.e., minimal terminal descent velocity. Experiments are performed on 3D-printed double-winged synthetic fruits for a wide range of wing fold angles (obtained from normalized curvature along the wing length), base wing angles, and wing loadings to determine how these affect the flight. Our experimental and theoretical models find an optimal wing fold angle that minimizes the descent velocity, where the curved wings must be sufficiently long to have horizontal segments, but also sufficiently short to ensure that their tip segments are primarily aligned along the horizontal direction. The curved shape of the wings of double winged autorotating diaspores may be an important parameter that improves the fitness of these plants in an ecological strategy.

DOI: 10.1103/PhysRevE.100.013108

I. INTRODUCTION

Wind dispersion of seeds is a widespread evolutionary adaptation found in plants, which allows them to multiply in numbers and to colonize new geographical areas [1–6]. Seeds, fruits, and other diaspores (dispersal units) are equipped with appendages that help generate a lift force to counteract gravity as they are passively transported with the wind. Seeds with a low terminal descent velocity increase their flight time and the opportunity to be transported horizontally by the wind before reaching the ground [7]. Many plant species are today unfortunately under severe stress and on the verge of becoming extinct due to climate change, timber extraction, and agricultural development [8]. The terminal velocity of the seed is a necessary prerequisite for accurate predictions from dispersion models [1,9], which can help predict their wind dispersion and influence policymakers in their conservation and reforestation plans [8]. Our recent work [10] suggests that whirling fruits can have evolved wings that indeed minimize their terminal descent velocity.

Since wind dispersal of seeds occupies a critical position in plant ecology, their flight organs have been carefully described along with their flight pattern [11–13]. These flight organs are often leaflike structures that function as wings, allowing the seed or diaspore to autorotate [12], tumble, or glide [11] as it is pulled to Earth by gravity. Other flight solutions are composed of thin-hairy structures such as the pappus on the dandelion [14], which effectively serves as a parachute. Common to all of these is the fact that their dispersion mechanisms rely on mechanical principles once they are released from the mother plant, a trait shared across plant species [15–19].

Single bladed autorotating seeds are often associated with maple trees and conifers, where the seed is attached to a single straight wing [13]. The delicate balance between the weight of the seed and the shape of the wing allows it to autorotate [20], leading to the production of an unexpectedly high lift [13]. Measurements of the air flow produced around autorotating *samaras* identify a leading edge vortex that is primarily responsible for the production of a positive lift force [21,22]. The seemingly simple configuration of having a single wing that generates a stable rotary descent has been widely studied [23–25], where recent work has shown that also the wing elasticity can influence the flight pattern [26] and may enhance lift [27,28]. Fossils from voltzian conifers dating back to the late early to middle Permian (ca. 270 Ma) are found to be double-winged [29]. This wing geometry is today vastly outnumbered by the autorotating single-winged morphology in the same plant family, which suggests that in the context of an ecological strategy the flight performance of single-winged seeds improves the fitness of their producers [29,30]. Pollen from the genus *Pinus* [31] have also been suggested to have evolved into shapes that improve their aerodynamic performance.

Autogyrating motion is also widely observed in multi-winged diaspores and seeds. These are commonly known as whirling fruits or helicopter fruits, which can be found in plant families such as Dipterocarpaceae [32–34], Hernandiaceae, Rubiaceae [35], and Polygonaceae, occurring in Asia, Africa, and the Americas. These fruits are equipped with a leaflike structure (persistent and enlarged sepals), which acts as wings in their rotary descent, illustrated in their Greek name, i.e., di = *two*, pteron = *wing*, and karpos = *fruit*. Compared to the single bladed maple fruits, these have a more complex wing shape, which curves upwards and outwards [36]. Only a limited subset of tropical whirling fruits are described in

*acarlson@math.uio.no

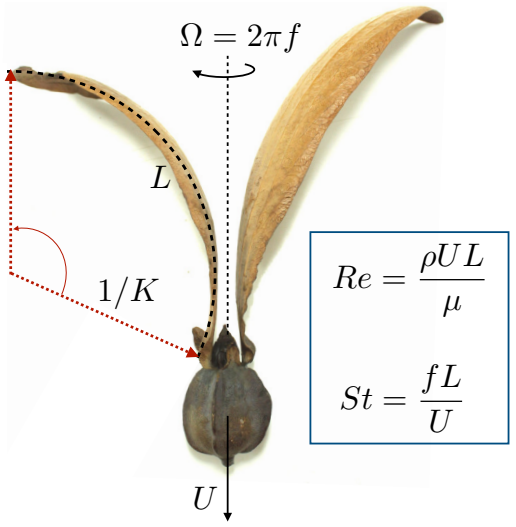

FIG. 1. We parametrize the shape of the fruit and its sepals, here illustrated by a dried fruit and wings from the dipterocarp family where we extract the sepal length (L) and notice that the sepal has a curvature K along the length of the wing here illustrated by fitting an osculating circle along the wing giving its radius of curvature $1/K$. The sepal's fold angle is defined as KL. The fluid has a density ρ and a viscosity μ. When the fruit is in free fall, it descends with a terminal velocity U and autogyrates with an angular frequency $\Omega = 2\pi f$, where f is the rotational frequency. Dimensional analysis gives us in addition to the fold angle KL, two nondimensional numbers that describe the flight; the Reynolds number (Re) is giving the ratio of inertia and the viscous force $\mathrm{Re} = \frac{\rho UL}{\mu}$ and the Strouhal number (St) is giving the ratio of the rotational speed and the translational speed $\mathrm{St} = \frac{fL}{U}$. Image courtesy of James Smith.

terms of their terminal descent velocity, as illustrated by the data from 34 neotropical trees [11], 53 recordings by Ref. [9], and recently extended by 16 entries of Paleotropic trees [32], which clearly limits predictions of dispersal distance. These flight recordings [11,32] suggest that the descent velocity is proportional to the square-root of the wing-loading, i.e., its mass divided by the disk defined by the projected wing area during rotation [6]. Recordings of the rotational frequency of this class of multi-winged fruits are elusive and essential to get a complete understanding of their aerodynamics. Besides our recent work [10], there are no studies, to the best of our knowledge, that characterize how the wing shapes of double-winged whirling fruits influence the terminal descent velocity and their rotational frequency. To understand the relationship between the wing geometry and the terminal descent velocity we deploy a methodology that combines 3D printing of synthetic fruits, experiments and a minimal theoretical description of their flight based on the blade element theory.

II. METHODOLOGY

A. Scaling analysis

One example of a whirling fruit from the dipterocarp family is shown in Fig. 1, which will autorotate as it descends. The angular frequency is $\Omega = 2\pi f$, where f is the rotational

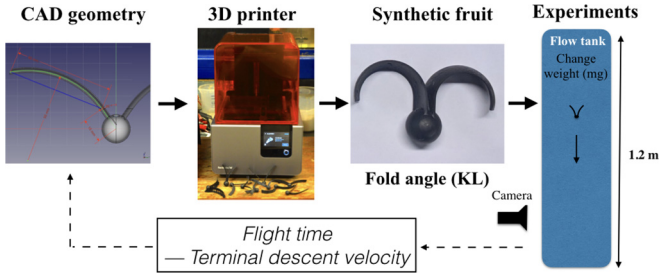

FIG. 2. Our experimental methodology and work flow is composed of digitalization of the synthetic fruits by a 3D Computer Aided Design model (FreeCAD v0.16), which is then 3D printed and used for flight experiments in a water tank. After varying the weight mg of each geometry by depositing a known weight of lead to its hollow fruit, we measure the terminal descent velocity U and rotational frequency f. After data evaluation we return to the CAD design with guidelines for the wing design, i.e., most significantly in this study the fold angle KL.

frequency and U is the terminal descent velocity. The sepals in Fig. 1 have a length L and a curvature K and the fruit is pulled to Earth by gravity with an acceleration g. Through dimensional analysis we define three nondimensional numbers; the Reynolds number (Re) is giving the ratio of inertia and the viscous force $\mathrm{Re} = \frac{\rho UL}{\mu}$, the Strouhal number (St) is giving the ratio of the rotational speed and the translational speed $\mathrm{St} = \frac{fL}{U}$, and the wings fold angle KL in radians. The fluid has a density ρ and a viscosity μ. The experiments and theoretical analysis are based on a flow with $\mathrm{Re} \gg 1$ and for steady descent, i.e., $U =$ constant, consistent with previous experiments on autorotating multi-winged fruits collected in the wild with $\mathrm{Re} \in 10^3 - 10^4$ [11,12,37] (see Table I). As the flow is dominated by inertia, we know then that the lift force scales as $|F_L| \sim C_L \rho U^2 A_d$ and the drag force scales as $|F_D| \sim C_D \rho U^2 A_d$ where C_L is the lift coefficient, C_D the drag coefficient and A_d is the area swept by the wing. To understand how U relates to the weight, we follow [12] by considering the mass flux through A_d and that the change in momentum must balance the weight of the fruit, giving the scaling law

$$U \propto \sqrt{mg/\rho A_d}. \tag{1}$$

Experiments on wild fruits show that individual groups [11,32] follow the scaling law Eq. (1), but they lack a description of how U is affected by the wing geometry.

B. Synthetic double-winged fruits

The workflow of our experimental approach is illustrated in Fig. 2. It consists in producing rapid prototyping synthetic fruits through 3D printing, then experimenting in a water tank to extract the terminal descent velocity (U) and the rotational frequency (f), which is evaluated and then fed-back to the design of a new wing geometry. A parametric 3D computer aided design model (CAD) is developed in FreeCAD v0.16 [38], see right part in Fig. 2 and CAD file (see the Appendix). The wing length from the base of the fruit to its tip is denoted by $L = 6\,\mathrm{cm}$ and the wing has a spanwise curvature along this direction. The fold angle KL, which is a geometric input

parameter to the CAD model and can be modified while keeping the total wing mass constant. The wing camber is set through a radius of curvature in the plane normal to the wingspan, and can also be adjusted without influencing the wing mass. We set a value for an effective additional angle of attack of 2.5° [see Eq. (4)] and the wing pitch angle $\alpha_p = 15°$, inspired by the geometry of the wings of wild fruits. It is very challenging to accurately measure the pitch and camber values from wild fruits, as these are strongly affected by their growth and the desiccation process. The angle ψ between the base of the wing and the vertical direction is chosen equal to $\psi = 0°$ or $\psi = 35°$, which encompasses the typical range of values observed in nature [10]. Finally, the fruit itself is designed as a hollow sphere with two holes, allowing us to vary its weight in experiments while keeping the volume fixed.

The synthetic fruits are produced by using the Form 2 3D printer from Formlabs [39], relying on the stereolithography technique with a print time of about 5 h for a batch of three fruits. This allows for rapid prototyping, and parametrization of fruit geometry as required for scanning a large phase space of shapes; see Fig. 2. Once the model is printed, it is cleaned in isopropanol, cured in UV light and polished to have a smooth surface before being used for experiments in the water tank.

C. Experimental design

We design our experiments so that both the Reynolds number (Re) and the Strouhal number (St) are in direct correspondence to fruit flight in Nature. The values for these parameters in our laboratory experiments correspond to those performed on wild fruits and are reported in Table I.

Experiments were performed in a cylindrical water tank of a height 1.2 m and a diameter 25 cm. A set of experiments were performed in a large water tank filled with water of depth 0.7 m, 0.5 m wide, and 10 m long, to make sure that wall effects are within the experimental error bars in the cylindrical tank. In the experiments, we control the amount of lead added to the hollow spherical fruit of the 3D-printed model and the additional volume is filled with water. The fruit is fully immersed under the water surface before it is released.

A camera is recording the motion of the fruit and wings from the side of the water tank at a frequency of 30Hz and a resolution of 864 × 480 pixels. Images are extracted from the video to track the fruit's lowest point and the wing tips. In our data analysis, we subtract the background to each image in the video, which makes the fruit to easily be identified and a combination of convolution filtering and thresholding is used to find the characteristic points; see Fig. 3 and the code for more details (see the Appendix). Calibration resorting to a third order polynomial is used to convert the position of the characteristic points in each image into the vertical position. The fruits rotational frequency is obtained by using a fast Fourier transform of the position of the wing tips, where the frequency is identified as the peak in the power-spectrum. To verify our post-processing analysis, we also performed

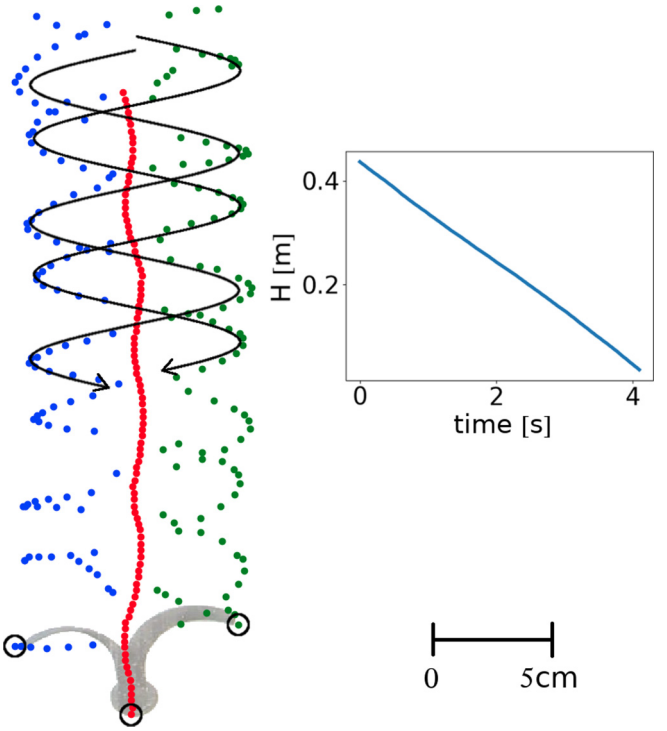

FIG. 3. The left part shows the raw data from our automatic tracking of the motion of a synthetic fruit, where we follow its wing tips and the vertical motion of the fruit. The lines are intended only as a guide to the eye to illustrate the motion of each individual wing. In the right part, we plot the vertical position H of the fruit in one part of the tank and show that our synthetic fruits reach a steady terminal descent velocity U.

TABLE I. Description of the parameters representative for the laboratory experiments and comparison with previously performed experiments on wild fruits from Ref. [37], where the rotation frequency f is not reported. The typical length of the sepals of wild fruits is estimated as $L = \sqrt{A_w}/2$, where A_w is the wing area reported in Ref. [37]. The value for St is estimated from Ref. [13] in the case of *Buckleya lanceolata* (Sieb. and Zucc.) Miq. [syn. *B. joan* (Sieb.) Makino (Santalaceae)] with a geometry similar to a *Dipterocarpus* fruit giving us the St number. The * symbol indicates that the numerical value could not be computed from the data reported in Ref. [37], but obtained from a species of similar shape [13].

Setup	f (Hz)	L (m)	U (m/s)	ν (m^2/s)	St	Re
Laboratory	0.4 to 2.4	0.06	0.04 to 0.2	1.0×10^{-6}	0.35 to 0.82	2400 to 14 000
Shorea argentifolia Symington (Dipterocarpaceae)	N/A	≈0.035	1.2	1.5×10^{-5}	0.40 (*)	2800
Shorea johorensis Foxw. (Dipterocarpaceae)	N/A	≈0.05	1.7	1.5×10^{-5}	0.40 (*)	5700
Shorea mecistopterix Ridl. (Dipterocarpaceae)	N/A	≈0.08	2.4	1.5×10^{-5}	0.40 (*)	12 700

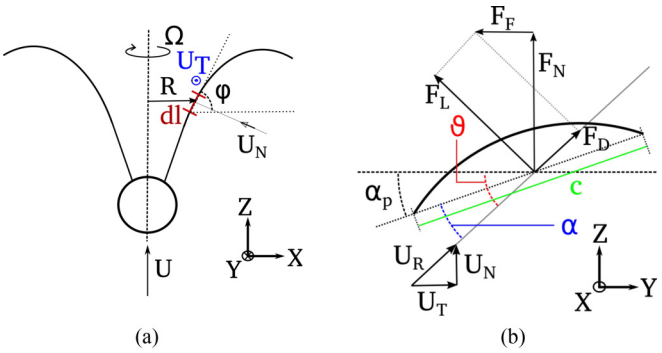

FIG. 4. (a) Sketch of the fruit's wings that are decomposed into small elements dl and moving with a frame of reference at the vertical descent velocity U. Ω is the rotation rate, dl the length of the blade element, R the distance of the blade element to the axis of rotation, ϕ the wing inclination at the location of the blade element, $U_N = U\cos(\phi)$ the normal component of the descent velocity, $U_T = R\Omega$ the tangential wind created by the rotation. (b) View of the blade element described in Fig. 4(a), in the plane perpendicular to the wingspan. c is the chord of the blade element, α_p its pitch angle, θ the angle of the relative wind, $\alpha = \theta - \alpha_p$ the angle of attack, U_R the wind speed "felt" by the blade element, L and D the lift and drag components, respectively, and F_F and F_N the resulting forward and vertical forces. The camber profile is illustrated by the curvature of the blade element.

measurements looking from the top and down into the water tank, which are found to be in excellent agreement with the measurements obtained by the side view. Each experiment is repeated ten times for $\psi = 0^\circ$ and three times for $\psi = 35^\circ$. All the reported data points are average values and the error bars is five times the standard deviation.

D. Blade element model

The blade element model gives a phenomenological description of the lift and torque generated by rotating wings [12,13,22] by considering the wing as a succession of small elements. For each element the relative wind, the local angle of attack, the lift force and the drag force are computed. Different from the scaling law in Eq. (1), the model helps illustrate where the principal components to the lift and drag force are generated on the wings.

The rotating fruit is parametrized [see Fig. 4(a)], with U the fruit's vertical descent speed, and Ω the rotation rate. For a given blade element of length dl, the inclination of the wing relative to the horizontal direction is ϕ so that the descent velocity has a projected component $U_N = U\cos(\phi)$ normal to the blade element. R is the distance between the blade element and the fruit's axis of rotation, so that the tangential velocity becomes $U_T = R\Omega$. In addition, ψ is the angle between the vertical direction and the wing base. $\psi = 0^\circ$, unless stated otherwise.

A view of the relative wind and the aerodynamic forces acting on the blade element in the plane perpendicular to the wingspan is shown in Fig. 4(b). α_p is the pitch angle of the blade element, c its chord, and the camber is visible through the curvature of the wing profile. The total relative wind at the blade element has a magnitude $U_R = \sqrt{U_T^2 + U_N^2}$, and is at an angle $\theta = \arctan(U_N/U_T)$ relative to the horizontal direction where the blade element's angle of attack is $\alpha = \theta - \alpha_p$. The lift force is the component of the aerodynamic force perpendicular to the direction of the relative wind, while drag is the force component parallel to the wind direction. The magnitude of the lift force $F_L = \frac{1}{2}\rho U_R^2 A C_L(\alpha)$ and the drag force $F_D = \frac{1}{2}\rho U_R^2 A C_D(\alpha)$ on an element are proportional to the lift and drag coefficients, $C_L(\alpha)$ and $C_D(\alpha)$ where $A = c \times dl$ is the area of the blade element.

The horizontal (forward) and normal forces, respectively, F_F and F_N, can therefore be obtained by projecting the total aerodynamic force obtained by the sum of lift and drag:

$$\begin{aligned} F_F &= F_L\sin(\theta) - F_D\cos(\theta), \\ F_N &= F_L\cos(\theta) + F_D\sin(\theta). \end{aligned} \tag{2}$$

As shown in Fig. 4(b), the horizontal force can be directed forward and act as a motor for the rotation of the wings. This takes place when the angle of the relative wind is large enough so that the forward projected component of the lift force exceeds the backward component of the drag force, i.e., close to the central axis of the fruit. This forward resultant force generates autorotation of winged fruits, in a similar way

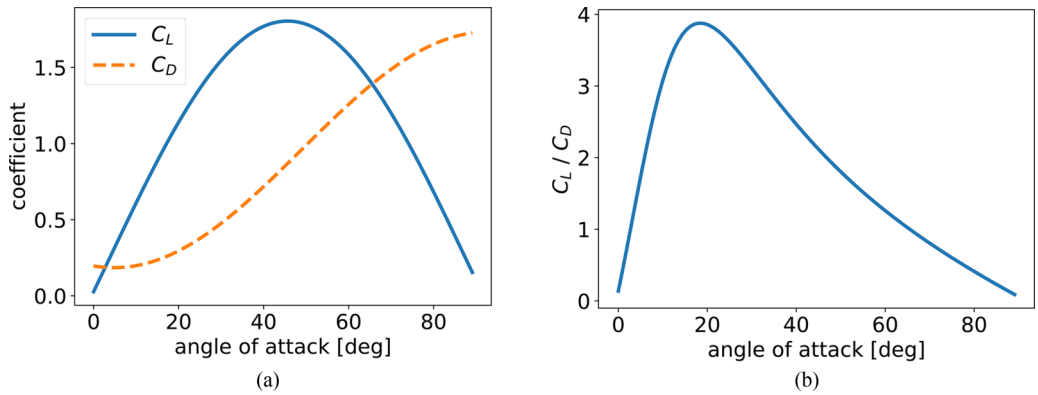

FIG. 5. (a) Parametrization used for the $C_L(\alpha)$ (solid line) and $C_D(\alpha)$ (dashed line) coefficients based on [43] using their Eqs. (12) and (13) but with $\max(C_D)/2$. A much smoother stall behavior is modeled compared with high Reynolds number wings, in agreement with studies performed for rotating wings at moderate Reynolds numbers where a strong leading edge vortex is present. (b) The parametrization results in a smooth shape for the $C_L(\alpha)/C_D(\alpha)$ curve.

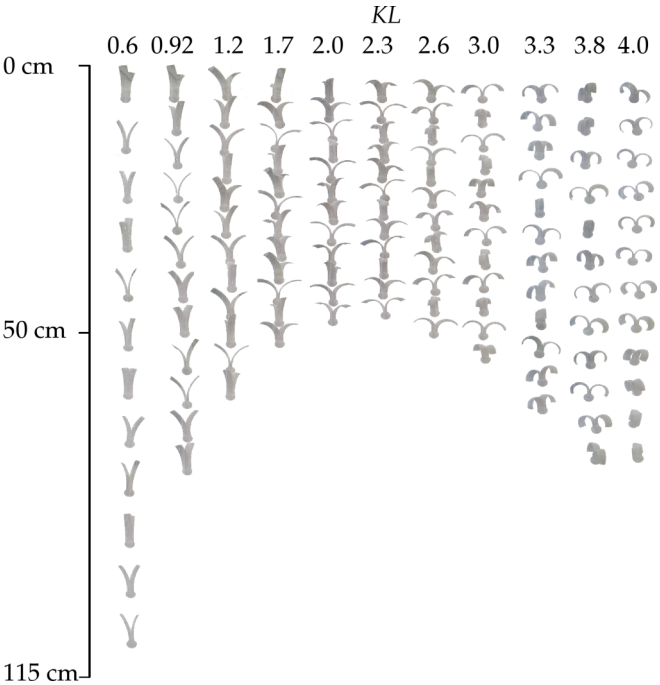

FIG. 6. Eleven 3D-printed synthetic double winged fruits with $\psi = 0^\circ$, $\Delta\alpha = 2.5^\circ$ and the same weight $mg = 20$ mN, but different fold angle KL are simultaneously released in the water tank. The image is a stroboscopic view of the path of the fruits and shows that the minimum terminal descent velocity is around $KL \approx 2.3$, in accordance with predictions of the blade element model [see Figs. 12(a) and 12(b)].

to what is used on a helicopter in autorotation [40]. As a consequence, a moment that drives autorotation is produced close to the axis of rotation of the fruit, while a moment that opposes rotation is produced close to the wing tips where the tangential velocity, and therefore drag, is the dominant horizontal force [12]. These quantities are further illustrated by the results shown in Fig. 11.

The total vertical force and torque acting on the fruit are obtained by integrating along the two wingspans and adding the effect of gravity, i.e., writing F the resulting vertical force, and M the moment around the rotational axis of the fruit,

$$F = 2\int_{l=0}^{l=S} F_N \cos(\phi) dl - mg,$$
$$M = 2\int_{l=0}^{l=S} F_F R dl, \tag{3}$$

where S is the total curvilinear length along the wingspan of one wing, R is the distance between the blade element and the vertical axis of the fruit, m the mass relative to the surrounding fluid, and g the acceleration of gravity.

Therefore, the predictions of the blade element model depend on two set of parameters; most importantly, the geometry of the wing, and also the lift and drag coefficients as a function of the angle of attack. This second part is arguably the most challenging to model accurately, as it is difficult to find tabulated values for the drag and lift coefficients of rotating wing segments at low to intermediate Reynolds numbers. This may come from a variety of reasons, including the small values of the forces acting on wing segments at the corresponding scales and Reynolds numbers in either air or water, which makes experimental measurements challenging. We have used two sets of parametrizations for the lift and drag coefficients; one from lift experiments on translating wing at slightly higher Reynolds numbers, and one inspired from rotating and flapping wings at similar Reynolds numbers as compared with our study. Both parametrizations qualitatively capture the trends in our experimental measurements.

For flat plates at high Reynolds number, the lift and drag coefficients can be obtained from both theoretical considerations (inviscid fluid flow with circulation together with the Kutta-Joukowski theorem, and boundary layer friction [41]) and experiments. These show that the lift force is a function of the angle of attack, i.e., $C_L(\alpha) = 2\pi \sin(\alpha)$ [41] and accurate until stall occurs, which for a flat plate usually arises at around $\alpha = 6^\circ$. In the case of low to intermediate Reynolds numbers, the behavior of $C_D(\alpha)$ and $C_L(\alpha)$ needs to be modified and we follow the results of Ref. [42], by using a maximum value of typical value $\max(C_L(\alpha)/C_D(\alpha)) = 7$

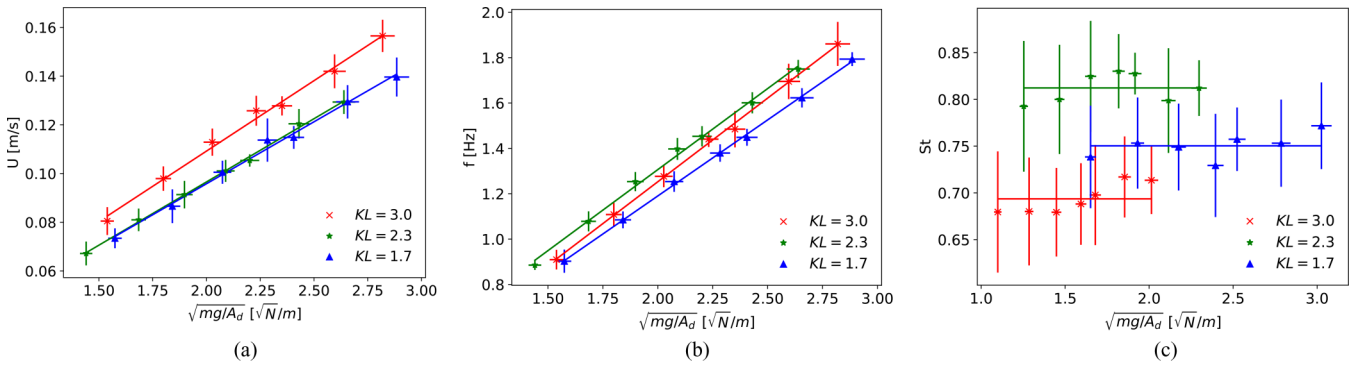

FIG. 7. We plot the experimental data for $\psi = 0^\circ$, $\Delta\alpha = 2.5^\circ$ for $KL = [1.7, 2.3, 3.0]$ where the wings span an area $A_d = [0.0058, 0.0069, 0.0061]m^2$, respectively. (a) The terminal descent velocity U is plotted as a function of the wing loading $\sqrt{mg/A_d}$, where we see that Eq. (1) does not collapse the data onto a single curve with respect to the scaled curvature KL where we want to note that the similarity of $KL = 1.7$ and $KL = 2.3$ is a special case. (b) The fruit's rotational frequency f is plotted as a function of $\sqrt{mg/A_d}$, where f is nonmonotonic with respect to the fold angle KL. (c) By rescaling U and f we plot the Strouhal number St, which is constant for each geometry but the magnitude of St is a function of KL.

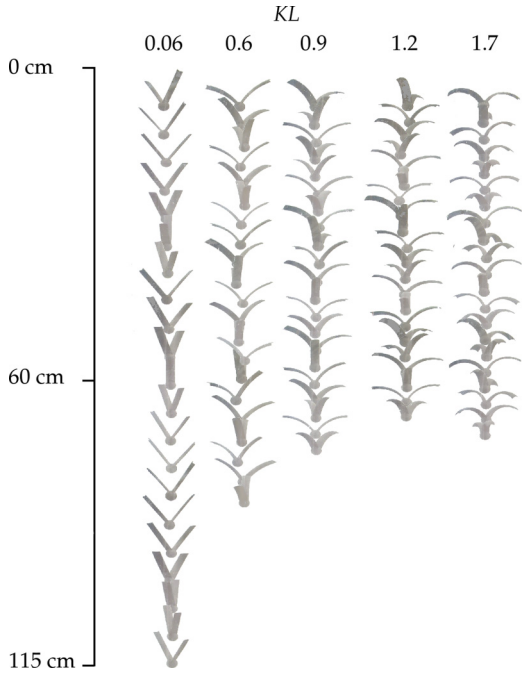

FIG. 8. Five 3D-printed synthetic double winged fruits with $\psi = 35^\circ$, $\Delta\alpha = 2.5^\circ$ and with the same weight $mg = 20\,\mathrm{mN}$, but with different fold angle KL are simultaneously released in the water tank. The image is a stroboscopic of the path of the fruits and shows that the minimum terminal descent velocity is around $KL = 1.2$, in accordance with predictions of the blade element model [see Figs. 12(c) and 12(d)].

before stall. This parametrization gives results in agreement with the experimental terminal descent velocity as a function of fold angle KL, and are also robust to changes in the peak value of C_L/C_D (see the Appendix). The Strouhal number around the optimal fold angle is also in good agreement with experiments. However, when one goes further away from the optimal fold angle, we find the stall behavior is likely too aggressive which explains the deviation from the experimental values for St; see the Appendix.

Indeed, experiments and simulations at Reynolds numbers comparable to the ones we experience indicate the existence of a strong leading edge vortex, that changes the stall pattern compared with higher Reynolds number [43,44]. Inspired by this observation we have also used another parametrization based on data from flapping wings reported by [43] using their Eqs. (12) and (13) from three-dimensional experiments, but with $\max(C_D)/2$, where no sharp stall is present and the lift coefficient increases up to a higher angle of attack than what is observed for flat plates at higher Reynolds numbers. However, compared to the results of Ref. [43], we reduce the value of the drag coefficient to $\max(C_D)/2$ to obtain agreement with our experiments. This may stem from the more complex shape of the wings in this study or the unsteady wing motion in Ref. [43]. In addition, the results presented here are for complete wings rather than an individual wing element, and therefore the relative values of drag obtained in Ref. [43] and similar works are probably larger than what is the case on individual wing elements far from the axis of rotation of our fruits. The parametrization is summarized in Fig. 5. We will only present results obtained from using the blade element model with a parametrization according to Fig. 5 in the main text and the additional simulations are in the Appendix, where we note that a precise curve for $C_D(\alpha)$ and $C_L(\alpha)$ would require a detailed flow measurements or high resolution computational fluid dynamics simulations, beyond the scope of this article.

We note that the wing camber also affects the lift generation by adding an offset to the lift coefficient curve [45], $C_{L,\mathrm{camber}}(\alpha) = C_{L,\mathrm{no\ camber}}(\alpha + \Delta\alpha)$. While this result applies primarily for higher Reynolds numbers than what we consider here, this is used as a first approximation of the behavior expected also in the present case. By considering a parabolic camber profile $\eta = \eta_0[1 - (2x/c)^2]$, with η the deviation between the chord line and the mean camber line and η_0 the maximum deviation at the middle of the wing chord, one obtains that [45]

$$\Delta\alpha = 4\pi\eta_0/c. \tag{4}$$

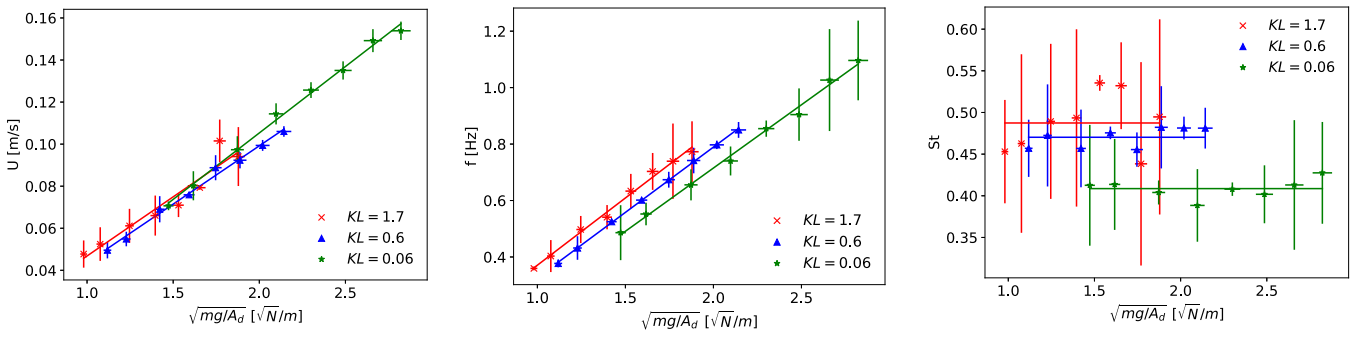

FIG. 9. We plot the experimental data for $\psi = 35^\circ$, $\Delta\alpha = 2.5^\circ$ for $KL = [0.06, 0.6, 1.7]$, where the wings span an area $A_d = [0.0053, 0.0092, 0.012]\,m^2$, respectively. (a) The terminal descent velocity U is plotted as a function of the wing loading $\sqrt{mg/A_d}$, where we see that Eq. (1) provides a fairly good description of U when the wings are not highly curved. (b) The fruit's rotational frequency f is plotted as a function of $\sqrt{mg/A_d}$, where f increases with the fold angle KL. (c) By rescaling U and f we plot the Strouhal number St, which is constant for each geometry but the magnitude of St is a function of KL.

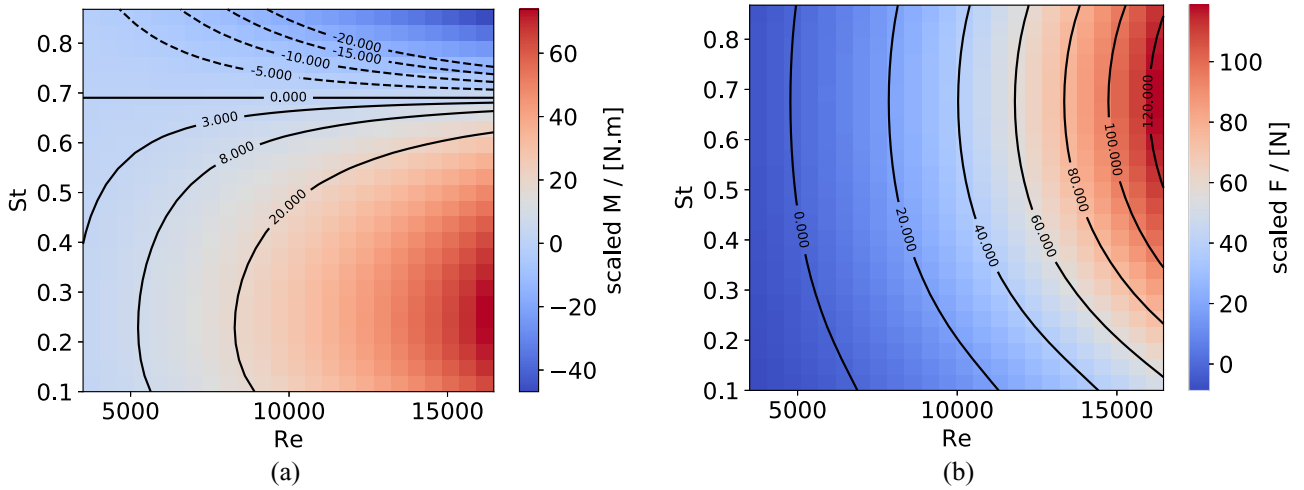

FIG. 10. 2D contour maps for (a) the moment M, and (b) the resultant vertical force F predicted by the blade element model Eq. (3) as a function of Re and St for the baseline fruit geometry, with a net mass loading of 1.2 g. The data presented in the figures are scaled of an arbitrary factor for ease of representation. The steady-state descent is obtained at $F = M = 0$, and it is stable as discussed in the text.

We use a circular camber profile that is equivalent to Eq. (4) as a first order approximation. In the explored parameter phase space the added angle of attack due to camber curvature is in the range of 0° to 4°. The blade element model obtained from Eqs. (2) and (3) is implemented in Python and solved numerically (see Ref. [46]). For each set of geometric parameters, vertical velocity U, and rotation rate Ω, the model computes the resulting moment M and vertical force F.

III. RESULTS

A. Experimental results

We have performed an extensive experimental parameter study where we systematically alter the base wing angle ψ, the fold angle KL, and the weight of the fruit by combining 3D printing of synthetic fruits and measurements in a water tank. The experimental phase space span; $KL \in [0\text{–}4]$ radians, $\mathrm{Re} \in [2.4\text{–}12] \times 10^3$, $\mathrm{St} \approx 0.1\text{–}0.9$, and $\psi = [0°, 35°]$.

1. Base wing angle $\psi = 0°$ and wing camber $\Delta\alpha = 2.5°$

We fix the base wing angle to $\psi = 0°$ and the wing camber $\Delta\alpha = 2.5°$, while we vary the weight mg and the fold angle KL in the experiments. To illustrate the flight paths of these synthetic fruits we show the stroboscopic photo in Fig. 6, where we have simultaneously released 11 3D-printed fruits at the same height and with the same weight in the water tank and track their descent distance for a fixed time $t = 5.5$ s. It is clear that there is an optimal geometry to maximise the flight

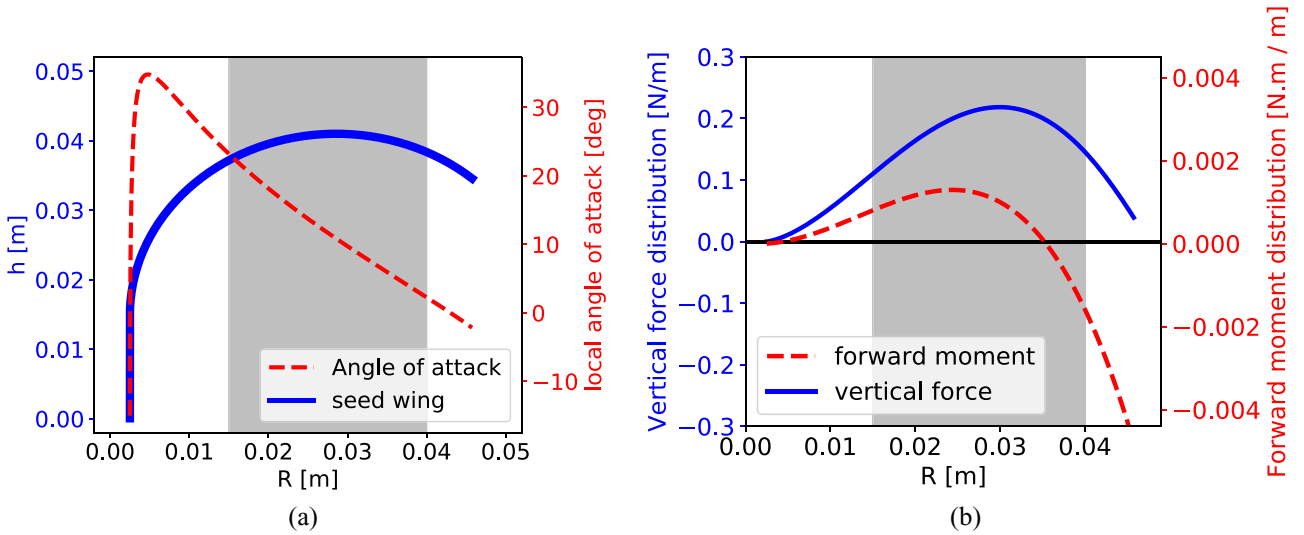

FIG. 11. (a) The cross section of the wing profile (left axis) corresponding to a synthetic fruit having fold angle $KL = 2.3$ as a function of the distance R between the blade element and the fruit's axis of rotation, and the corresponding angle of attack in the stationary regime (right axis). The part of the wing where significant lift is created is highlighted in gray, (b) the corresponding distribution of vertical force (left axis) and driving momentum (right axis).

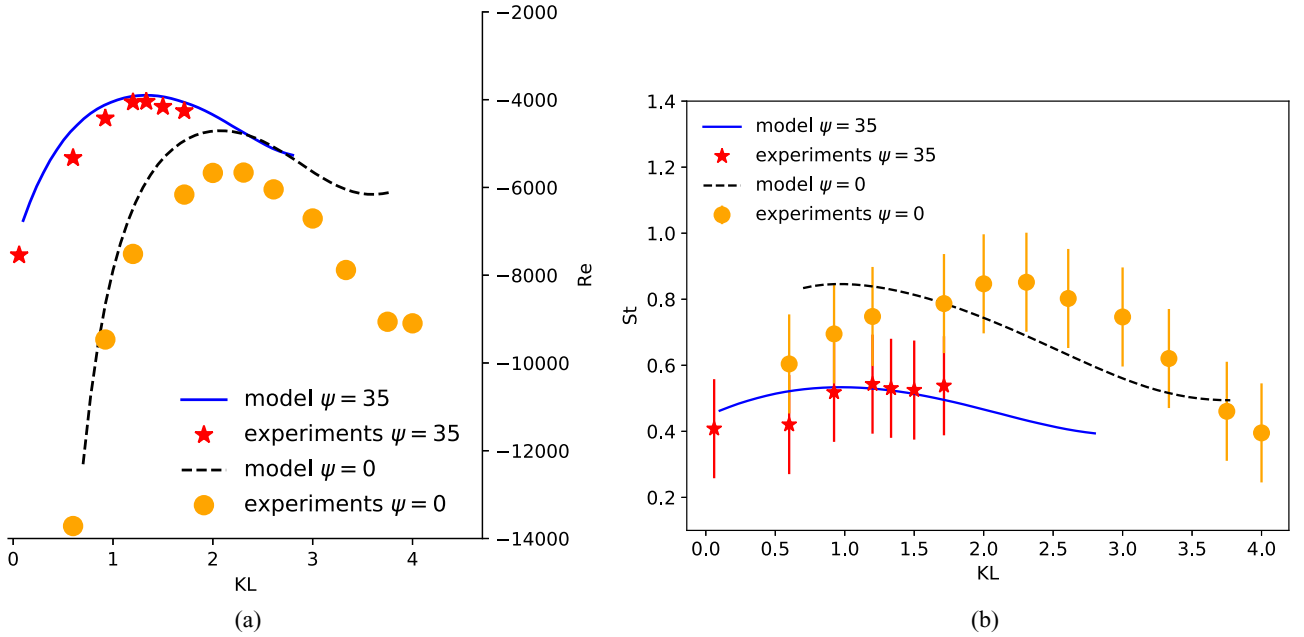

FIG. 12. (a) We solve the blade element model using the parametrization shown in Fig. 5, for the two series of seeds already presented in Figs. 6 and 8. The experimental data is shown by the markers, which illustrates that the fold-angle KL is the essential parameter to obtain a minimal terminal descent velocity that would suggest optimal wind dispersion potential, as previously discussed. Good agreement is found regarding the general shape of the curves, the position of the optimal KL for each base angle ψ, and the relative change of falling velocity observed between Figs. 6 and 8. (b) We show the Strouhal number St, for the same set of seeds. Here, satisfactory agreement is found when considering the simplicity of the model. Both the typical magnitude of St in each case, the effect of modifying the base angle ψ, and the general trend of St with respect to KL are satisfactorily reproduced by the model.

time. We have compared the fold angle of these synthetic fruits with 27 species that reside in Africa, Asia, and the Americas where they were collected in the wild, which are found to have a fold angle mean$(KL) = 1.8 \pm 0.18$, close to the optimum. This suggests that similar wing shapes have evolved in Nature and indicates that aerodynamic performance, i.e., minimal descent velocity, may improve the fitness of these plants in an ecological strategy.

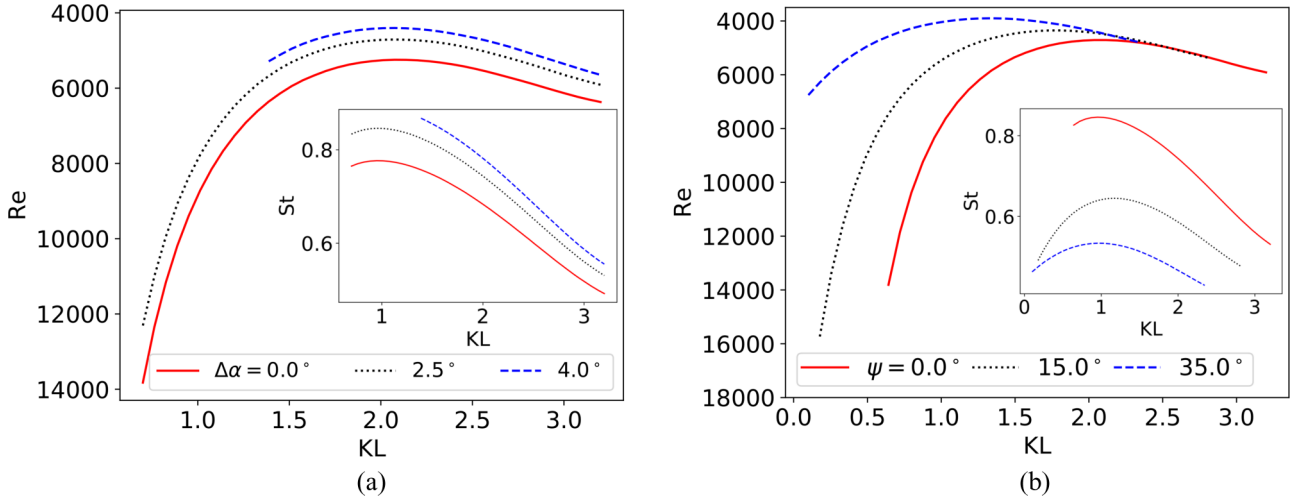

FIG. 13. (a) The terminal descent velocity and Strouhal number as a function of sepal camber ($\Delta\alpha$) and sepal fold angle, as predicted by the blade element model for $\Psi = 0°$. The addition of a camber does not affect the placement of the minimal descent velocity along the KL axis, but only influences its magnitude. This is due to improved autogyration, as visible through the inset for the Strouhal number. (b) Changes in the base angle ψ formed between the base of the wing and the vertical axis shift the placement of the minimal descent velocity on the KL axis, which is moved to smaller KL when ψ increases. Simultaneoulsy, a larger ψ leads to a larger projected wingspan which increases the relative wind created due to rotation on the outer part of the wings, which in turn reduces the equilibrium Strouhal number.

InFigs. 7(a)–7(c) the measured terminal descent velocity U, the rotational frequency f and the St number are plotted as a function of the wing loading $\sqrt{mg/A_D}$ for three fold angles. It is clear from Fig. 7(a) that the scaling law in Eq. (1) does not fully capture the influence of the fold angle KL as it does not collapse the data onto a single curve, but illustrates that for each individual wing geometry the terminal descent velocity scales as $\sim\sqrt{mg}$, consistent with experiments on wild fruits [11,32]. The rotational frequency f is also a function of KL and by replotting U and f through $\mathrm{St} = fL/U$ we see that for each geometry St is constant [see Fig. 7(c)]. Thus, our experiments follow the predictions from the blade element model and our theoretical analysis [see next section, Eq. (5)]. Note that the error-bar in St is ≈5% and accumulated from the measurement error in both U and f. As there is a clear coupling between KL and U we are curious to determine if there is a geometry that minimizes the terminal descent velocity, which we argue to be optimal in terms of the seeds dispersion potential.

2. *Base wing angle $\psi = 35°$ and wing camber $\Delta\alpha = 2.5°$*

Fruits and seeds can also have wings with an attachment/base angle ψ that is not necessary zero. To understand how ψ influences the terminal descent velocity we performed additional measurements with $\psi = 35°$, $mg = 19\,\mathrm{mN}$, and $\Delta\alpha = 2.5°$ where we vary mg and KL. A stroboscopic image of these flight paths are shown in Fig. 8 for a fixed mass and flight time $t = 5.5$ s, to further illustrate the relationship between the KL and U. Compared with the case when $\psi = 0°$ we notice that the optimal fold angle has decreased, with a minimum terminal descent velocity obtained near $KL \approx 1.2$.

Similar to $\psi = 0°$, we see that there is an influence in U and f as a function of KL [see Fig. 9(a)]; however, the influence is not as pronounced for these smaller fold angles where the wings are not that highly curved and Eq. (1) predicts U reasonably well. By rescaling U and f through St, we notice that it is constant for each geometry but the magnitude depends on KL. Experiments with additional wings, but keeping the total wing area constant were found to only make a slight change in Re and St numbers, and as such we did not include these here.

B. Blade element model

We solve the blade element model for the synthetic fruit with a model geometry with $\psi = 0°, \alpha_p = 15°$ and with an effective mass loading of 1.2 g. The data is presented in nondimensional 2D contour maps for F and M as presented in Fig. 10. The dependence of the angle of attack, forward moment, and vertical force on the position along wingspan for a fruit with a fold angle of $KL = 2.3$ is shown in Fig. 11.

In Fig. 10 the level line for zero total moment is straight, corresponding to a constant Strouhal number St, only determined by the geometry of the fruit wings. This is consistent with all our experiments [Figs. 7(c) and 9(c)], and can be seen in the blade element model from Eq. (3) by substituting the value of F_F:

$$M = \int_{l=0}^{l=S} \frac{1}{2}\rho U_R^2 A[C_L(\alpha)\sin(\theta) - C_D(\alpha)\cos(\theta)]Rdl. \quad (5)$$

Using a constant St implies that the relative wind direction, and therefore angle of attack α, remains constant for each blade element. Therefore, if the fruit is experiencing a zero mean torque, changing the descent speed for a given fruit geometry and St will result in replacing U_R by a scaled value in Eq. (5) while keeping all other terms constant, i.e., the resulting moment M will still be zero. This result is independent of the parametrization used for both $C_L(\alpha)$ and $C_D(\alpha)$.

To find the terminal descent velocity and rotation rate of the falling fruit, we need to determine the parameters [U, Ω], in nondimensional form, [Re, St] for which the total resultant vertical force F and the resulting moment M are zero. This is done numerically, based on an analysis of the 2D maps for both quantities. The equilibrium point is stable, as confirmed by the experimental measurements. Indeed, as visible in Fig. 10, for a large St we get a negative moment, i.e., a reduction of St, while a small St leads to a positive moment, i.e., an increase of St, implying that the fruit returns to equilibrium. Similarly, the vertical force increases with a large descent velocity U, i.e., a large Re number, leading to an upwards resulting force that slows down the vertical motion of the fruit, and opposite for a small descent velocity leading to a large downwards resulting force, which will increase the descent speed. Direct comparison between the experimental results and the predictions from the blade element model show that they are in good agreement, given the phenomenological nature of this model (Fig. 12).

To demonstrate the sensitivity in geometrical changes in the wing, we show in Fig. 13 the effect of both $\Delta\alpha$ and ψ on the minimal terminal descent speed as predicted by the blade element model. The camber $\Delta\alpha$ has no influence on the placement of the minimal terminal descent velocity along the KL axis, but only influences the magnitude of the descent velocity as it increases/decreases the effective lift force. The base angle ψ in Fig. 13(b) has both a limited influence on the minimal terminal descent velocity, and shifts the position along the KL axis, consistent with our experiments see Figs. 6 and 8: a larger ψ leads to smaller value fold angle KL to ensure a minimal descent velocity.

Indeed, for a fixed weight we see that as we start with a KL value close to 0 and gradually increase the fold angle the descent velocity U is being reduced; see Fig. 12. For $\psi = 0$ a minimal U is identified for $KL \approx 2.0$ and as we further increase $KL > 2.0$ the descent velocity starts to increase. We can in part understand the placement of these optimal fold angles if we infer that the total force in the vertical direction will scale with the projected length of the wing on the horizontal axis as seen from Eq. (1). However, this cannot alone explain the shift in minimal terminal descent speed as shown in Fig. 7(a). As KL increases so does the wing swept area and the wing tip approaches an approximately horizontal shape. Near the peak in the KL-Re the wing tip is close to being horizontal, and as KL increases the horizontal part on the wing moves toward the wing base/fruit, which then

reduces the relative velocity as R is smaller along with the vertical lift force, although the wing swept area is nearly the same. The wing shape must also influence how vortices are shedded, which generate circulation and lift. Therefore, these curved wings must be sufficiently long to have horizontal segments, but also sufficiently short to ensure that their tip segments are primarily aligned along the horizontal direction. However, the exact optimum for the fold angle KL is a result of the complex interplay between the flow and the wing geometry.

IV. CONCLUSIONS

We have presented an experimental study and a minimal phenomenological flow model encompassing the main physical ingredients of the flight of synthetic whirling fruits, which mimic those found in nature. Our results point to geometrical shapes of the wings of multi-winged seeds, fruits and diaspores, which provide them with an optimal dispersion potential, i.e., maximal flight time, and compares favourably with wing geometries found in the wild [10]. For whirling fruits to maximize the time they are airborne, their appendages that function as wings must not curve too much or too little. Our methodology consists of a combination of rapid prototyping by 3D printing, a minimal theory and experiments, and may be adopted for other studies of how wing geometry affects flight, which may help understand the evolutionary links between form and fitness of flight organs found in Nature.

ACKNOWLEDGMENTS

We are very thankful to James Smith, Jaboury Ghazoul, Yasmine Meroz, Renaud Bastien, and Anneleen Kool for stimulating discussions about *Dipterocarpus* fruits and for their valuable input on this work. We thank Olav Gundersen for the assistance with developing the experiment design. We gratefully acknowledge financial support from the Faculty of Mathematics and Natural Science, and the UiO:LifeScience initiative at the University of Oslo.

APPENDIX

1. Source files: CAD files, images of wild fruits, and the numerical code solving the blade element model

Additional material including the baseline CAD file used for performing the parametric analysis, the images of wild fruits with osculating circle, and the code to solve the blade element model, is available at Ref. [46].

2. Results from the blade element model with $C_D(\alpha)$ and $C_L(\alpha)$ inspired by flat plate measurements

In this Appendix, we present the results obtained by using a parametrization with stall inspired from translating wings at slightly higher Reynolds (Re) numbers as described in the main section of the text [43,44], corresponding to the C_L and C_D coefficients from Fig. 14 [47–49]. Results are obtained by solving the blade elements model, in the same way as in the article. As visible in Fig. 15, the curves for the Re number are in good agreement with the experiments, however overall the results obtained with the parametrization inspired from rotating wings at smaller Re numbers. The Strouhal (St) number is also mostly following the trends observed in experiments, though the discrepancy with the experiments is larger than what was reported in Fig. 12, especially for $\psi = 0$ when the strong stall takes place (high values of KL). Finally, the results for the terminal Re number are found to be insensitive to the peak value of $C_L(\alpha)/C_D(\alpha)$, as shown in Fig. 16.

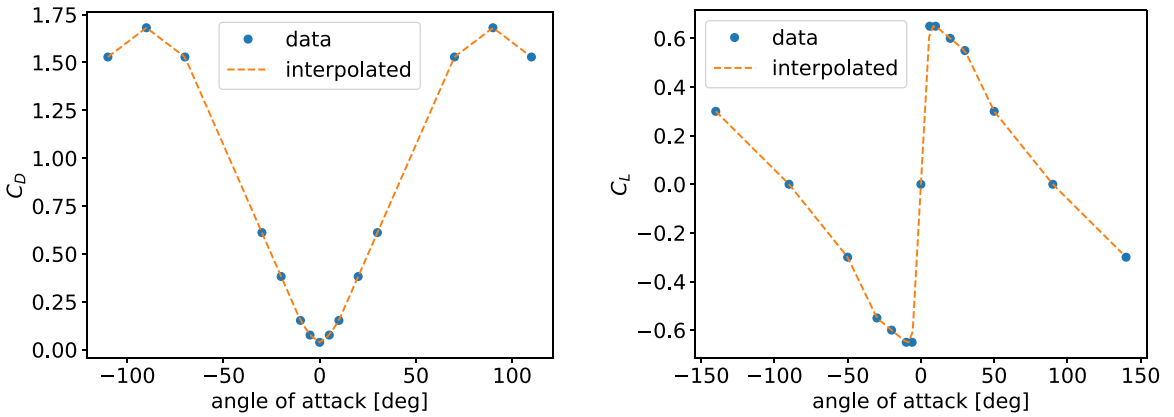

FIG. 14. Parametrization for (a) $C_D(\alpha)$ and (b) $C_L(\alpha)$ inspired from translating wings at slightly higher Re numbers. A sharp stall behavior is present for an angle of attack of around 6°.

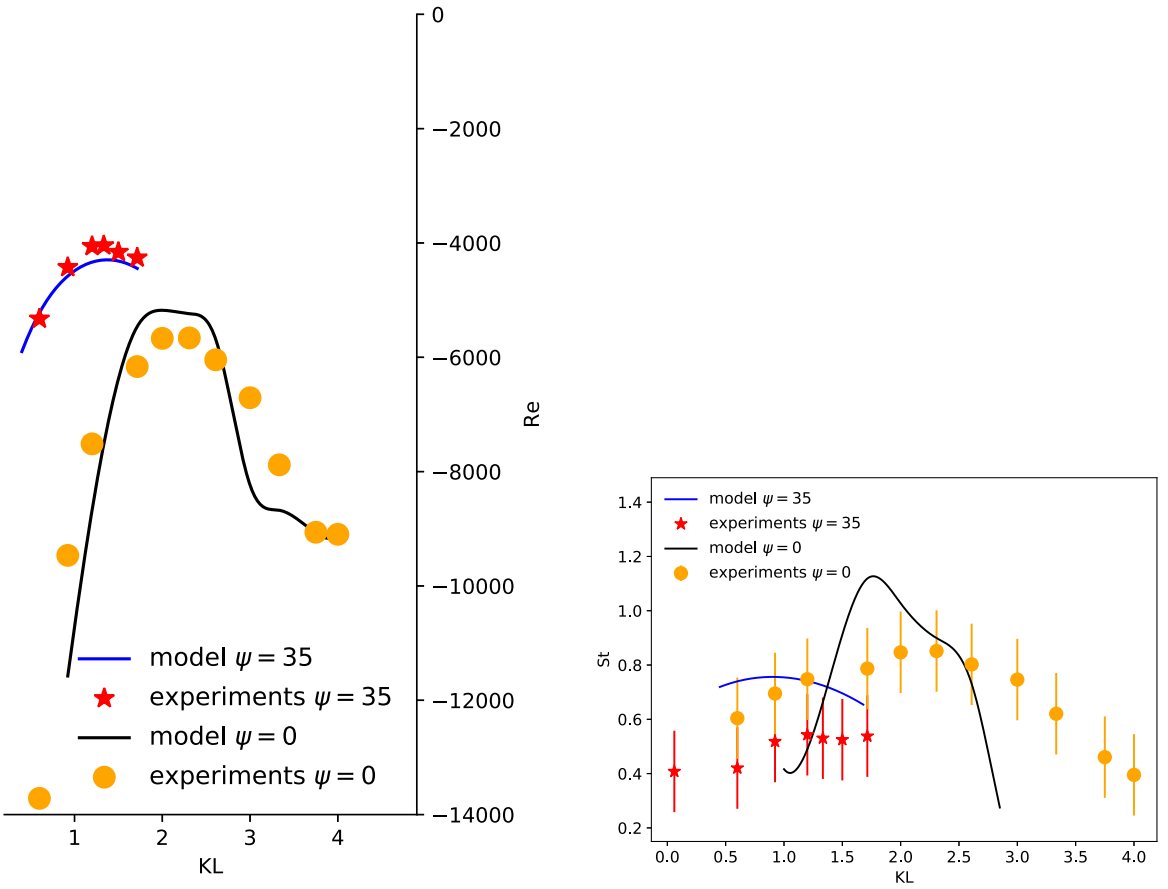

(a) (b)

FIG. 15. Comparison between experimental results with synthetic 3D-printed biomimetic fruits and the blade elements model, using the parametrization of Fig. 14. The results are in reasonable agreement for the terminal velocity [Reynolds number, panel (a)]. The results for the Strouhal number [panel (b)] follow the same trend as the experimental results, though the agreement is not as good as in Fig. 12, especially at higher values of KL when stall takes place.

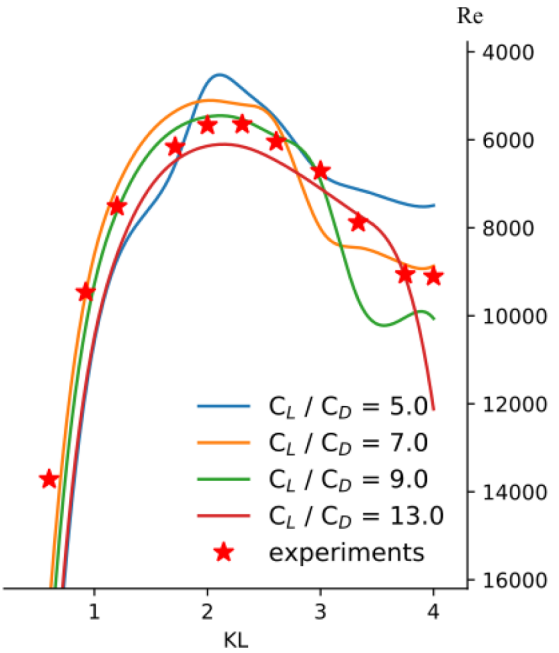

FIG. 16. Influence of varying the peak value of $C_L(\alpha)/C_D(\alpha)$ for the parametrization inspired by translating wings. While the details of the curves shape are altered, the position of the optimum curvatures remains mostly unchanged.

[1] N. Ran, Long-distance dispersal of plants, Science **313**, 786 (2006).

[2] H. N. Ridley, *The Dispersal of Plants Throughout the World* (L. Reeve and Co., London, 1930).

[3] H. F. Howe and J. Smallwood, Ecology of seed dispersal, Annu. Rev. Ecol. Syst. **13**, 201 (1982).

[4] N. Ran, F. M. Schurr, O. Spiegel, O. Steinitz, A. Trakhtenbrot, and A. Tsoar, Mechanisms of long-distance seed dispersal, Trends Ecol. Evol. **23**, 638 (2008).

[5] M. L. Cain, B. G. Milligan, and A. E. Strand, Long distance seed dispersal in plant populations, Am. J. Bot. **87**, 1217 (2000).

[6] D. F. Greene and E. A. Johnson, A model of wind dispersal of winged or plumed seeds, Ecology **70**, 339 (1989).

[7] O. Tackenberg, P. Poschlod, and S. Kahmen, Dandelion seed dispersal: The horizontal wind speed does not matter for long distance dispersal, Plant Biol. **5**, 451 (2003).

[8] J. Ghazoul, *Dipterocarp Biology, Ecology, and Conservation* (Oxford University Press, Oxford, 2016).

[9] R. Tamme, L. Götzenberger, M. Zobel, J. M. Bullock, D. A. P. Hooftman, A. Kaasik, and M. Pärtel, Predicting species' maximum dispersal distances from simple plant traits, Ecology **95(2)**, 505 (2014).

[10] J. Rabault, R. A. Fauli, and A. Carlson, Curving to Fly: Synthetic Adaptation Unveils Optimal Flight Performance of Whirling Fruits, Phys. Rev. Lett. **122**, 024501 (2019).

[11] C. K. Augspurger, Morphology and dispersal potential of wind-dispersed diaspores of neotropical trees, Am. J. Bot. **73**, 353 (1986).

[12] R. Norberg, Autorotation, self-stability, and structure of single-winged fruits and seeds (samaras) with comparative remarks on animal flight, Biol. Rev. **48**, 561 (1973).

[13] A. Akira and Y. Kunio, Flight performance of rotary seeds, J. Theor. Biol. **138**, 23 (1989).

[14] C. Cummins, M. Seale, A. Macente, D. Certini, E. Mastropaolo, I. M. Viola, and N. Nakayama, A separated vortex ring underlies the flight of the dandelion, Nature **562**, 414 (2018).

[15] R. Elbaum, L. Zaltzman, I. Burgert, and P. Fratzl, The role of wheat awns in the seed dispersal unit, Science **324**, 884 (2007).

[16] P. Marmottant, A. Ponomarenko, and D. Bienaimé, The walk and jump of Equisetum spores, Proc. Roy. Soc. B **280**, 20131465 (2013).

[17] J. M. Skotheim and L. Mahadevan, Physical limits and design principles for plant and fungal movements, Science **308**, 1308 (2005).

[18] X. Noblin, N. O. Rojas, J. Westbrook, C. Llorens, M. Argentina, and J. Dumais, The fern sporangium: A unique catapult, Science **335**, 1322 (2012).

[19] S. Armon, E. Efrati, R. Kupferman, and E. Sharon, Geometry and mechanics in the opening of chiral seed pods, Science **333**, 1726 (2011).

[20] K. Varshney, S. Chang, and Z. J. Wang, The kinematics of falling maple seeds and the initial transition to a helical motion, Nonlinearity **25**, C1 (2012).

[21] D. Lentink, W. B. Dickson, J. L. Van Leeuwen, and M. H. Dickinson, Leading-edge vortices elevate lift of autorotating plant seeds, Science **324**, 1438 (2009).

[22] S. J. Lee, E. J. Lee, and M. H. Sohn, Mechanism of autorotation flight of maple samaras (acer palmatum), Exp. Fluids **55**, 1718 (2014).

[23] T. H. Smith, Autorotating wings—An experimental investigation, J. Fluid Mech. **50**, 513 (1971).

[24] L. Mahadevan, W. S. Ryu, and A. D. T. Samuel, Tumbling cards, Phys. Fluids **11**, 1 (1999).

[25] U. Pesavento and Z. J. Wang, Falling Paper: Navier-Stokes Solutions, Model of Fluid Forces, and Center of Mass Elevation, Phys. Rev. Lett. **93**, 144501 (2004).

[26] D. Tam, J. W. M. Bush, M. Robitaille, and A. Kudrolli, Tumbling Dynamics of Passive Flexible Wings, Phys. Rev. Lett. **104**, 184504 (2010).

[27] D. Tam, Flexibility increases lift for passive fluttering wings, J. Fluid Mech. **765**, R2 (2015).

[28] K. Varshney, S. Chang, and Z. J. Wang, Unsteady aerodynamic forces and torques on falling parallelograms in coupled tumbling-helical motions, Phys. Rev. E **87**, 053021 (2013).

[29] A. R. Stevenson, D. Evangleista, and C. V. Looy, When conifers took flight: A biomechanical evaluation of an imperfect evolutionary takeoff, Paleobiology **2**, 205 (2015).

[30] D. L. Contreras, I. A. P. Duijnstee, S. Ranks, C. R. Marshall, and C. V. Looy, Evolution of dispersal strategies in conifers: Functional divergence and convergence in the morphology of diaspores, Perspect. Plant Ecol. Evol. System. **24**, 93 (2017).

[31] S. A. Cain, The identification of species in fossil pollen of pinus by size-frequency determinations, Am. J. Bot. **27**, 301 (1940).

[32] J. R. Smith, R. Bagchi, J. Ellens, C. J. Kettle, D. F. R. P. Burslem, C. R. Maycock, E. Khoo, and J. Ghazoul, Predicting dispersal of auto-gyrating fruit in tropical trees: a case study from the Dipterocarpaceae, Ecol. Evol. **5**, 1794 (2015).

[33] E. Suzuki and P. S. Ashton, Sepal and nut size ratio of fruits of asian dipterocarpaceae and its implications for dispersal, J. Trop. Ecol. **12**, 853 (1996).

[34] G. R. Matlack, Size, shape, and fall behavior in wind-dispersed plant species, Am. J. Bot. **74**, 1150 (1987).

[35] J. van Staden, K. Kelly, and C. Stormanns, Dormancy and germination of alberta magna seeds, S. Afr. J. Bot. **56**, 542 (1990).

[36] D. Attenborough, *The Private Life of Plants: A Natural History of Plant Behaviour* (BBC Books, London, 1995).

[37] J. R. Smith, R. Bagchi, C. J. Kettle, C. Maycock, E. Khoo, and J. Ghazoul, Predicting the terminal velocity of dipterocarp fruit, Biotropica **48**, 154 (2016).

[38] J. Riegel, W. Mayer, and Y. van Havre, Freecad (version 0.16), http://www.freecadweb.org (2001–2017).

[39] FormLabs, Form2, https://formlabs.com.

[40] J. Shapiro, *Principles of Helicopter Engineering* (McGraw-Hill, New York, 1956).

[41] L. D. Landau and E. M. Lifshitz, *Fluid mechanics* (Elsevier, Amsterdam, 2013), Vol. 6.

[42] P. B. S. Lissaman, Low-reynolds-number airfoils, Annu. Rev. Fluid Mech. **15**, 223 (1983).

[43] Z. J. Wang, J. M. Birch, and M. H. Dickinson, Unsteady forces and flows in low Reynolds number hovering flight: Two-dimensional computations vs robotic wing experiments, J. Exp. Biol. **207**, 449 (2004).

[44] D. Lentink and M. H. Dickinson, Rotational accelerations stabilize leading edge vortices on revolving fly wings, J. Exp. Biol. **212**, 2705 (2009).

[45] J. N. Newman, *Marine Hydrodynamics* (MIT Press, Cambridge, MA, 1977).

[46] Repository with baseline CAD file, images of real-world seeds, and a simple blade element model to analyze the effect of wing fold angle on the flight dynamics of autorotating seeds, https://github.com/jerabaul29/EffectFoldAngleAutorotatingSeeds.

[47] J. McArthur, Aerodynamics of wings at low Reynolds numbers: Boundary layer separation and reattachment Ph.D. Dissertation, University of Southern California, California, 2008.

[48] G. K. Ananda, P. P. Sukumar, and M. S. Selig, Measured aerodynamic characteristics of wings at low Reynolds numbers, Aerosp. Sci. Technol. **42**, 392 (2015).

[49] X. Ortiz, D. Rival, and D. Wood, Forces and moments on flat plates of small aspect ratio with application to PV wind loads and small wind turbine blades, Energies **8**, 2438 (2015).